THz Prism: One-Shot Simultaneous Localization of Multiple Wireless Nodes With Leaky-Wave THz Antennas and Transceivers in CMOS

Hooman Saeidi, *Graduate Student Member, IEEE*, Suresh Venkatesh, *Member, IEEE*, Xuyang Lu, *Member, IEEE*, and Kaushik Sengupta, *Senior Member, IEEE*

Abstract—In this article, we propose and demonstrate a spectrum-to-space mapping principle for localizing multiple wireless nodes in a simultaneous and single-shot fashion at terahertz (THz) frequencies. Spectrum-to-space mapping is achieved through two dual-port chip integrated waveguide (CIW)-based leaky-wave antennas (LWAs). Interfacing with the two LWAs, we integrate two transmitting and receiving chains operating between 360- and 400-GHz range in a single chip realized in a 65-nm bulk CMOS process. Utilizing the carefully engineered dispersive nature of the LWA and its frequency-dependent radiation patterns, we create unique spectrum-to-space calibration maps for both 1-D and 2-D angular localizations. The measured one-shot localization error variance is less than 1° in 1-D space with 200-Hz-resolution bandwidth (BW) and less than 2° in 2-D space for a 20-Hz-resolution BW. The high-resolution nature of the localization principle in a single-shot fashion makes this approach attractive for multi-wireless node localization, link discovery, beam-forming, beam-management, and beam-optimization methods.

Index Terms—5G, antenna, beam management, beamforming, chip integrated waveguide (CIW), CMOS, frequency multiplier, leaky-wave antenna, link discovery, localization, substrate integrated waveguide (SIW), terahertz (THz), traveling wave antenna, waveguide.

I. INTRODUCTION

THERE is significant growth expected in the number and the density of connected devices as the network transformation continues with 5G and beyond. To accommodate the heterogeneous need for connectivity, including multi-Gb/s wireless links, newer bands in the millimeter-wave (mm-Wave) and terahertz (THz) above 100 GHz are attracting attention for applications in communication for augmented and
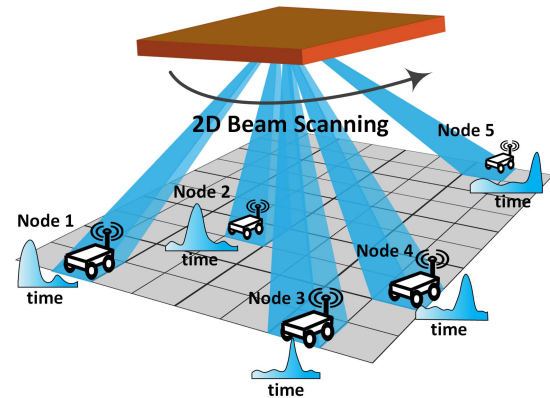
Fig. 1. Conventional node localization approach with directive beams at mmWave/THz showing beam-optimization across multiple links established through iterative scanning in 2-D space.

virtual reality and for intelligent sensing and imaging systems in autonomous vehicles, robotics, and cyber–physical systems [1]–[5]. These applications are expected to be supported through a heterogeneous and dynamically reconfigurable network fabric for future wireless communication [1], [6]–[10].

Migrating to higher frequencies in the mm-Wave and THz regime requires the wireless links to be highly directive to overcome the path loss, either in an indoor or an outdoor environment [11]–[13]. Establishing a directed beam to close the wireless link requires angular localization [14]. To allow for low latency communication, rapid localization, direction finding, and tracking of multiple mobile wireless nodes are critical [5], [15]–[26]. In 5G new radio, to establish a new wireless link between the two nodes, beam optimization is enabled through an iterative process. One approach, as shown in Fig. 1, relies on the transmitter–receiver (Tx–Rx) pair to search for all possible beamforming codes in the set to find the optimal ones for the link with the highest signal-to-noise ratio (SNR). For N possible codes for each of the Tx and Rx, this brute-force search has a complexity of $O(N^2)$. One approach to reduce the search complexity is that one of the nodes (either Tx or Rx) has a quasi-omni-directional beam pattern, and the other side scans the space through the N possible beam positions to find the best beam direction. Afterward, the scanning is done on the other side and repeated, leading to a complexity order reduction to $O(N)$. A recently proposed method of localization in [27] relies on the transmission of multiple simultaneous beams across different settings. Through careful
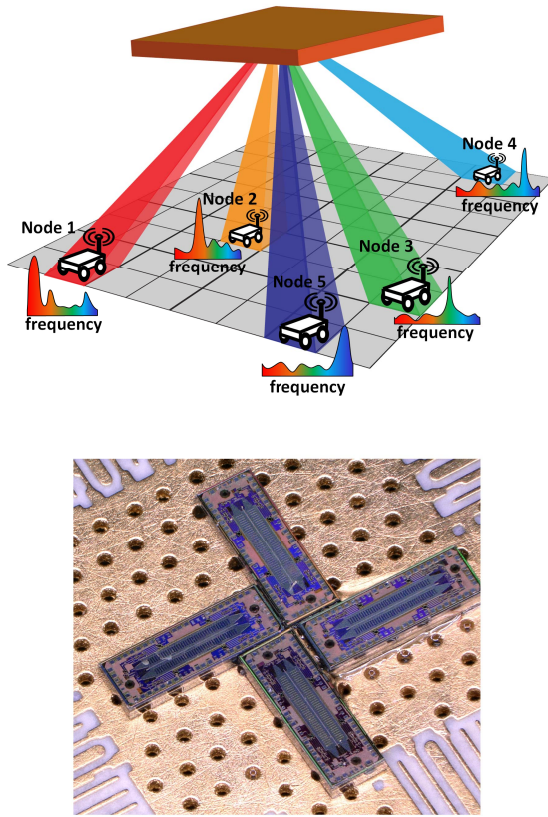
Fig. 2. THz Prism and 2-D spectrum-to-space mapping principle demonstrating localization of multiple nodes established in a single-shot simultaneous fashion through measurements of the local incident spectrum. The figure also illustrates a possible realization of 2-D angular coverage with four THz Prism chips with integrated 1-D LWAs.

evaluation of the received signal with overlapping settings and agile-link beam hashing approach, this complexity can be reduced to $O(K \log N)$, where N is the total number of angular locations and K is the number of paths traveled by the signal in each hashing. Each of these iterative approaches has its distinctive tradeoffs among different metrics, such as latency, energy consumption, and achievable optimal SNR.

This work takes a different approach where the localization information is extracted at the "edge" node through local measurement of the ambient spectrum that the transmitter uniquely projects onto the space, eliminating the need for time-intensive iterative beamforming optimization. The conceptual figure is shown in Fig. 2 in which the access point (AP) acts as the "THz Prism" that creates a unique spectrum-to-space mapping through the emission of different frequency components toward different angular locations in the space. While the principle is applicable across the electromagnetic spectrum, we choose THz to demonstrate the proof-of-concept for its ability to resolve localization information with high angular resolution [28]. Utilizing the uniqueness of the spectrum-to-space mapping, multiple edge nodes can simultaneously localize themselves in a single-shot fashion through localized spectrum sensing. This can allow us to circumvent the latency bottleneck for the iterative beam scanning process, establishing one-shot optimal beam-forming codes across multiple wireless nodes. Furthermore, the control plane algorithm to accommodate the addition of a new wireless node is simplified as

the location can be sensed at the edge and communicated to the AP.

Here, by utilizing integrated dual-port leaky-wave antennas with on-chip transceivers, we demonstrate spectrally dependent radiation beams across 360–400 GHz covering $\pm\,40°$ in transmitting and receiving modes. Through orthogonal placements of these chips, we show a scalable architecture approach toward enabling the 2-D localization of wireless nodes. The system has less than $1°$ measured error variance for 1-D angular localization with 200-Hz-resolution bandwidth (BW) and less than $2°$ measured error variance for 2-D angular localization with a 20-Hz-resolution BW, when measured at a distance of 5 cm. The optimal choice of frequency needs to be carefully chosen keeping in mind the radiator aperture size (that determines the frequency-dependent directivity of the beams), generated transmitter power, receiver sensitivity, and the measurement range. Here, we choose the frequency range of 360–400 GHz as determined by the aperture area of the antenna realized in a 3-mm^2 size chip. If operated at a lower frequency and an equivalently larger aperture area, a similar resolution can be obtained at higher power (and, therefore, higher range). The design choices need to be optimized based on the application and the desired specifications.

The measurement distance can evidently be increased with an array implementation. By arraying N elements on the centralized THz prism, the EIRP can be increased by a factor of N^2 [29]. For the same level of received SNR, the range can be enhanced by the factor of N. As an example, with a 10×10 element Tx array, the distance can be enhanced to 5 m, making it suitable for a wide range of applications. The distance can be further increased with an array (albeit smaller) at the client side. While the preliminary results were presented in [30], here, we present a detailed analysis of the architecture, circuits, antenna, and measurement results. The broadband transceivers integrated into the chip along with the effective use of frequency dispersive radiators make this approaches extremely attractive for node localization, wireless link discovery, and beam-optimization methods.

This article is divided as follows. In Section II, we present the concept of THz Prism, single-shot localization using spectrum to space mapping principles, and the conceptual implementation of the proposed system. The chip integrated waveguide (CIW) and the leaky-wave antenna are presented in Section III. The transmitter and receiver architectures, circuits schematic, and design are presented in Section IV. Measurement results of the antenna properties, transmitter and receiver performances, and localization measurements in both 1-D and 2-D are presented in Section V.

II. THz PRISM: SINGLE-SHOT LOCALIZATION PRINCIPAL USING FREQUENCY DISPERSIVE ANTENNAS

The principle of establishing angular location information from measured spectrum relies on frequency dispersive antennas where injected frequencies are emitted toward different angular locations, as illustrated in Fig. 3. Such spectrally dependent radiation patterns can be enabled through a leaky-wave antenna (LWA) [28], [31]. Such structures have
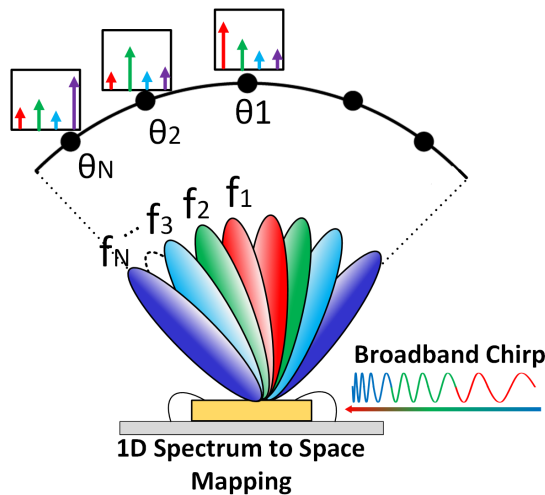
Fig. 3. Unique spectrum to angular mapping by injecting a broadband pulse or chirped frequency into an on-chip LWA that radiates different frequencies toward different angular locations.
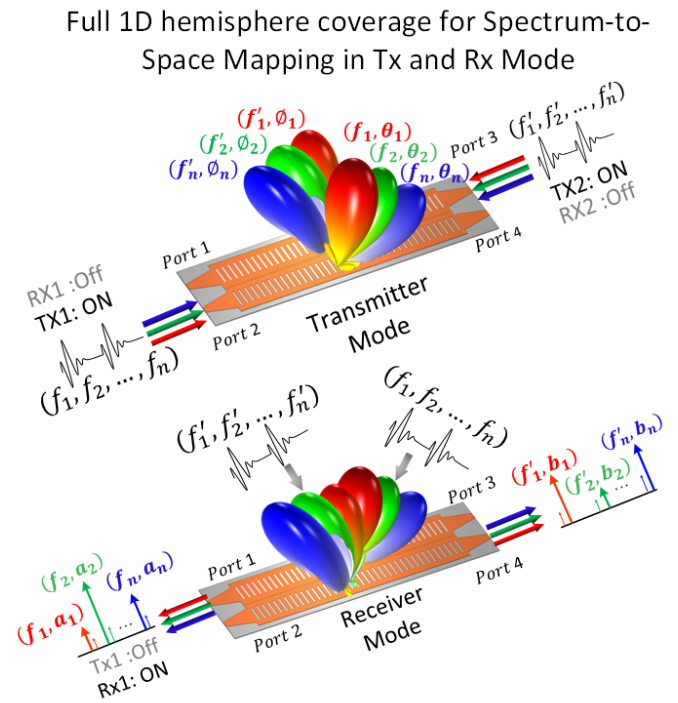

Fig. 4. Full 1-D hemisphere coverage using two dual-port integrated LWA with integrated THz transceivers at both ports of each LWA for transmitting and receiving operations.
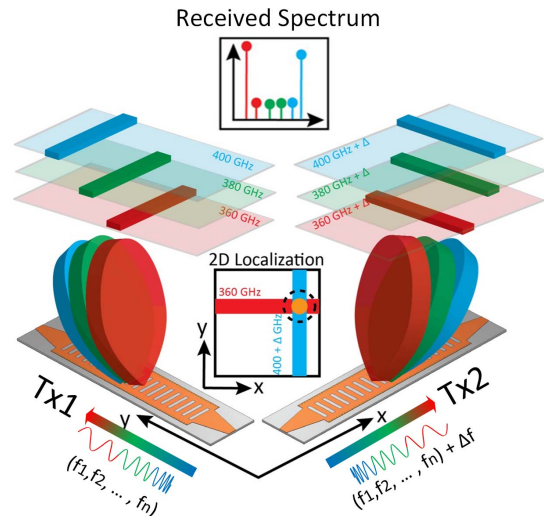

Fig. 5. 2-D angular localization with two orthogonal chips and integrated LWAs excited with a frequency offset to create a unique spectrum-to-space mapping.

been demonstrated at microwave and mm-Wave frequencies with fabricated planar antennas on printed-circuit boards, particularly leveraging substrate integrated waveguide (SIW) structures [32]–[35]. At THz, such interfaces have been previously demonstrated in custom fabricated parallel-plate leaky-waveguide structures [28], in silicon [36], and with III–V waveguide-based modules [31].

As we will elaborate later, the antennas need to be designed to allow fast-propagation waves through the structure. This allows the traveling wave to leak energy in the form of radiation through the spectrally dependent patterns. The radiation pattern varies from almost broadside (lower frequencies) to endfire (high frequencies) and covers one quadrant of the spatial angles, as shown in Fig. 4. For full 1-D hemispheric coverage, another LWA with an antenna fed from the opposite direction is needed. To create unique spectrum-to-space mapping, we can incorporate slightly offset frequencies between the two injected signals to the two antennas, as shown in Fig. 5. In this work, we incorporate both transmission and reception capability of spectrally dependent patterns in the chip to allow for flexible deployment of the Tx/Rx systems, as shown in Fig. 4. In the transmit mode, broadband frequencies can be injected from Port 2 and Port 3 for full 1-D hemisphere coverage. In the receiving mode, Port 1 and Port 4 are enabled. Due to the radiative nature of the LWA, the two end ports of an LWA are isolated by more than 15 dB across 360–400-GHz operation. The two LWAs are isolated by more than 35 dB as they are separated by a via wall. This allows potential operation in a full-duplex mode of operation. In this work, we integrate two such CIW-based antennas and transceivers on-chip covering a 360–400-GHz range of operation.

To allow for 2-D localization, we can utilize two orthogonally placed sources with a small frequency shift between them for unique 2-D coverage, as illustrated in Fig. 5. A wireless node can deduce its angular relation in a 3-D space based on the received spectrum with the prior knowledge of the spectrum-to-space map created by the THz Prism.

III. DUAL-PORT INTEGRATED LEAKY-WAVE ANTENNA

LWAs have the ability to radiate the beams that scan throughout the space as a function of the radiated frequency. The LWAs belong to the class of traveling wave antennas and are realized through modification of the conventional waveguiding structures. The unique frequency scanning capability is realized by designing the waveguiding structure to leak out the energy as the wave propagates down the antenna. The key design objective lies in controlling the leakage that allows the desired mode to radiate out. Such structures have been
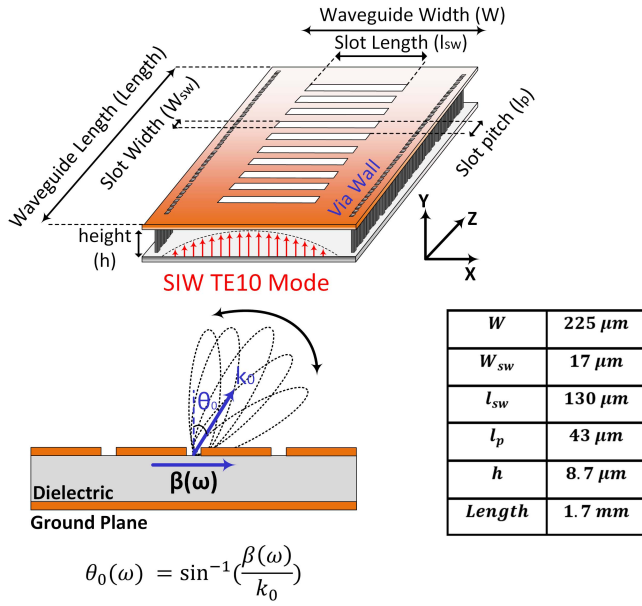
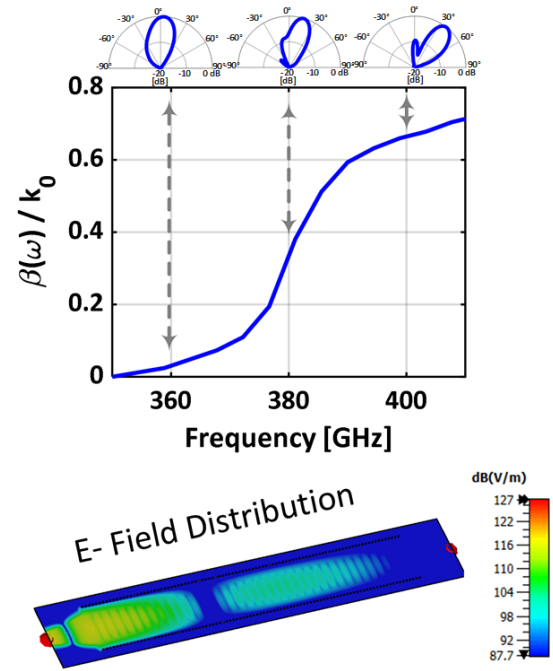Fig. 6. CIW with transversal slots to realize leak-wave operation at THz.

Fig. 7. Simulated dispersive nature of the wave propagation in the waveguide leading to spectrally dependent radiation patterns. The figure also shows the simulated electric field distribution of the propagating wave.

demonstrated with SIWs [33], [35], [37]–[42] for seamless integration with planar circuits and interfacing with microstrip transmission lines.

The structure of the on-chip waveguide-based leaky antenna is shown in Fig. 6. The waveguide is realized on the top 1.45-μm-thick metal in the 65-nm process for a net spacing of 8.7 μm between the top and bottom metal plates. The waveguide width is designed have the following geometries: $L = 1.7$ mm, $W = 225$ μm, sloth length (l_{sw}) $= 130$ μm, sloth width (W_{sw}) $= 17$ μm, and slot pitch (l_p) $= 43$ μm (see Fig. 6). The leaky-wave mode operates in the fundamental TE$_{10}$ mode. As the wave traverses along the length of the antenna, it leaks out energy through the periodic set of transverse slots that interrupt the current flow [35]. The dispersive nature of the propagation changes the radiation pattern as the frequency changes, allowing the forward scan to increase in the frequency. The design of these parameters controls the dispersive behavior of the LWAs, including frequency of operation, radiation efficiency, and scanning range.

An LWA supports three overall propagation modes that include a leaky-waveguide mode, a bounded non-leaky-waveguide mode, and a surface-wave mode. Close to the TE$_{10}$ cutoff frequency, the leaky-wave mode dominates over the surface-wave modes. The periodic nature of the slotted waveguide results in the multiple possible Floquet modes. To realize the desirable dispersion engineering across 360–400 GHz, the leaky-wave propagating along the z-direction can be expressed by the propagation constant k_{zn} of the nth space harmonic

$$E_y(\omega) = A(x)e^{-jk_{\text{zn}}z} \qquad (1)$$

where $A(x) = E_0 \sin(\pi x/W)$ and $k_{\text{zn}} = k_z + 2n\pi/l_p$ define the propagation constant of the nth space harmonic [35].

The propagation constant of the wave in the z-direction is related to radial propagation constant $k_{\rho n}$ of the radiated signal of the nth space harmonic as

$$k_{\rho n} = \sqrt{k_0^2 - k_{\text{zn}}^2} \qquad (2)$$

where $k_0 = \omega(\mu_0 \epsilon_r \epsilon_0)^{1/2}$, and μ_0, ϵ_0, and ϵ_r represent, respectively, the magnetic permeability, dielectric permittivity of free space, and relative dielectric permittivity of the waveguide dielectric.

The slot pitch of the LWA is designed to be small to allow the $n = 0$ as the radiating mode, while the other space harmonics are forced to be evanescent. Also, the small slot width ensures the preservation of the polarization of the radiated wave.

The radiation pattern of the LWA with N identical slots can be evaluated as

$$f(\theta) = \sum_{i=1}^{N} L_n e^{-jk_z l_p} e^{jk_0 l_p \cos\theta} \qquad (3)$$

where L_n is the length of the nth slot. The radiation pattern calculation allows us to calculate the scanning angle or radiation beam maxima as a function of the frequency as

$$\theta_0(\omega) = \sin^{-1}\left(\frac{\beta(\omega)}{k_0}\right). \qquad (4)$$

Here, we represent the complex propagation constant $k_z = \beta(\omega) - j\alpha(\omega)$, where $\beta(\omega)$ defines the wavenumber of the propagating wave and $\alpha(\omega)$ is the attenuation constant as the wave leaks out radiative energy. The variation of the radiation pattern due to the dispersion characteristics is elaborated in Fig. 7.
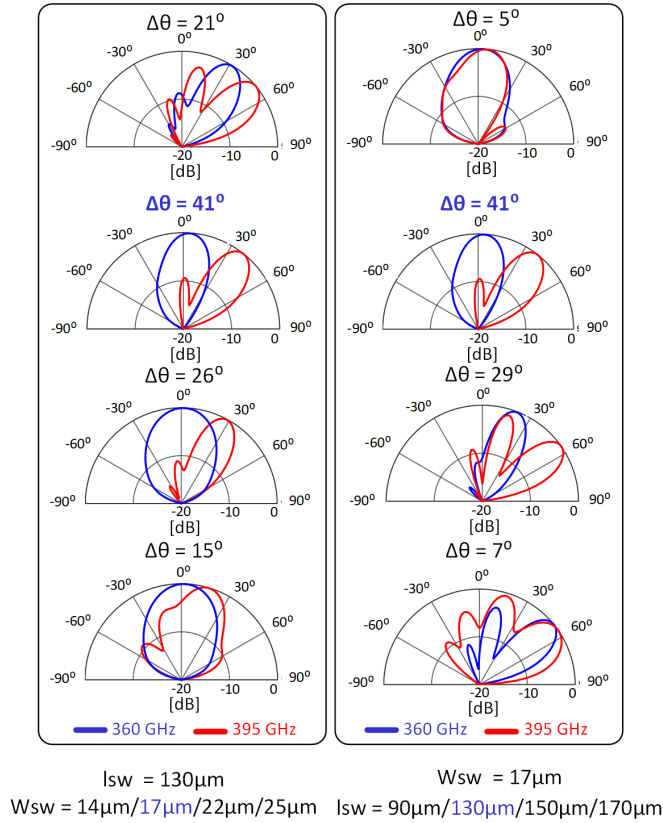
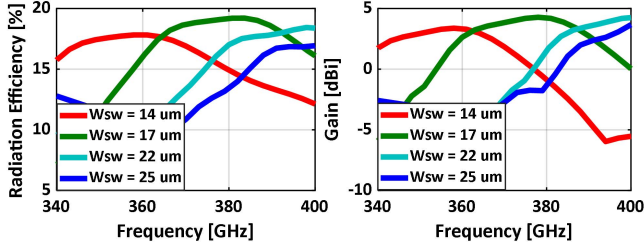Fig. 8. Simulated radiation patterns for different slot lengths and widths.

Fig. 9. Simulated radiation efficiency and the gain of the antenna across the operating frequency for different slot widths.

The beamwidth is related to the length of the LWA that is proportional to its aperture

$$\theta_{3dB} \approx \frac{\lambda_\circ}{L\cos(\theta)}. \tag{5}$$

The dispersion relation of $\beta(\omega)$ in (4) demonstrates that the forward scanning is achieved when the waveguide sustains a fast wave within the structure maintaining

$$\beta(\omega) < k_0. \tag{6}$$

The length of the antenna is typically chosen in such a way that most of the energy leaks out before it reaches the opposite port. The power reaching the opposite port can be given as

$$P_{\text{leakage}} = \left(1 - e^{-2\alpha L}\right). \tag{7}$$

The term α is a function of both α_r and α_{rad} that represent, respectively, the attenuation constants representing the copper loss in the waveguide and radiative loss due to leakage. For an efficient radiator, the goal is to enhance the ratio $\alpha_{\text{rad}}/\alpha_{\text{loss}}$.
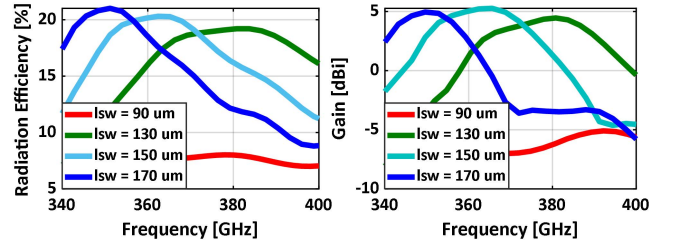

Fig. 10. Simulated radiation efficiency and the gain of the antenna across the operating frequency for different slot lengths.
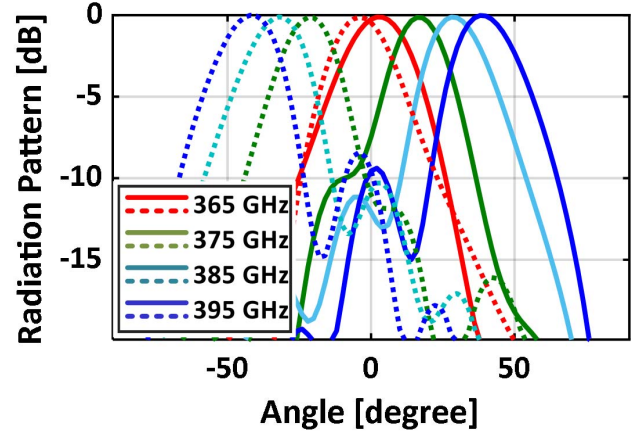
Fig. 11. Simulated radiation patterns for different frequencies across the band. Solid lines correspond to the feeding from left-hand side, while the dashed lines correspond to the feeding from right-hand side.
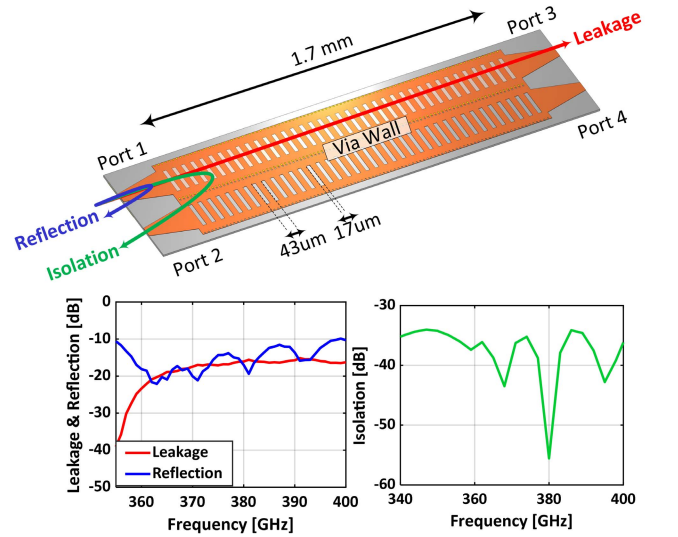
Fig. 12. Simulated scattering parameters of the two dual-port LWA across the frequency.

The first design consideration of the CIW is the width of the waveguide (W) (see Fig. 6). The width should be chosen to set the lower cutoff frequency of the fundamental TE_{10} mode below the desired operating frequency range. For a dielectric (with relative dielectric permittivity ϵ_r) filled waveguide operating in the TE_{10} mode, the cutoff frequency f_c can be calculated as

$$f_c = \frac{c}{2W\sqrt{\epsilon_0\epsilon_r}}. \tag{8}$$

Fig. 13. Integrated THz Prism architecture across 360–400 GHz, including two transmitting chains, two receiving chains, and two dual-port CIW-based LWAs.

Here, we choose $W = 225$ μm that sets the lower cutoff frequency to 325 GHz. The dispersion engineering across the frequency of interest 360–400 GHz is achieved by suitable choices of the slot width (W_{sw}), the slot length (l_{sw}), and the slot pitch (l_p).

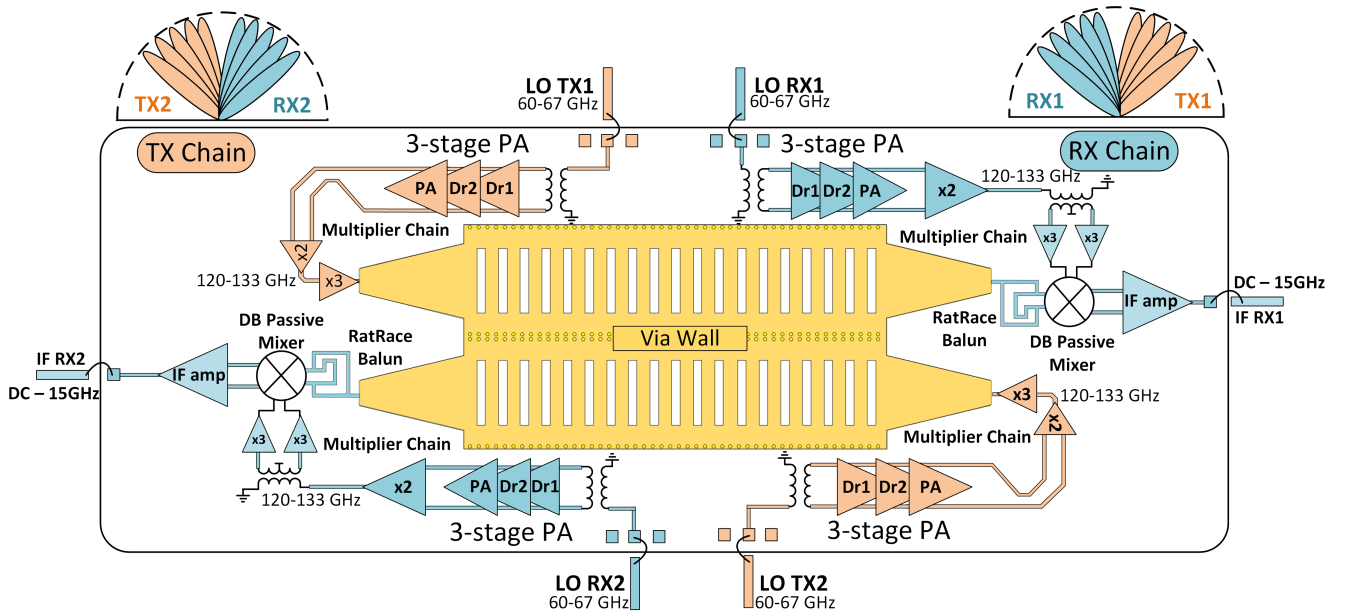The simulated radiation patterns of the LWA for various choices of slot length and slot width are shown in Fig. 8. The pattern coverage is governed by the dispersion relation (4) that is related to the design parameters of the transversal slots. The radiation efficiency and gain of the LWA for these geometries are shown in Figs. 9 and 10. At the low end, as the frequency approaches toward the cutoff frequency of the waveguide, α_{loss} increases drastically compared to α_{rad} due to the material loss that leads to a significant reduction in gain and efficiency of the radiating structure. In addition, at the high end of the frequency, as the β/k_0 gets close to unity, or equivalently when it approaches toward endfire, the contribution of the surface wave increases [33]. In that regard, the radiation contribution ($\alpha_{rad}/\alpha_{loss}$) reduces, which leads to a reduction of both efficiency and gain of the antenna.

As can be seen from the figures, design choices of slot length (l_{sw}) and slot width (W_{sw}) of 130 and 17 μm, respectively, create the optimal dispersion engineering across 360–400 GHz allowing coverage radiation over a 40°. Such sub-wavelength spacing of the slot width and slot spacing $\lambda/10$ (43 μm) ensures the preservation of the polarization [35]. In order to provide the capability to full 1-D hemispherical coverage, we incorporate two LWAs that are excited from opposite ends. For this design, the radiation patterns as a function of frequency, by exciting the two ports, are shown in Fig. 11. The designed antenna has a peak radiation efficiency of 19% with a peak gain of 4.5 dBi.

The THz transmitter and receivers can be integrated on the two opposite ends of the LWA (Tx: Port 1 and Port 4 and Rx: Port 2 and Port 3 in Fig. 12). As shown in Fig. 12,

the taper allows broadband matching where the input reflection coefficient is less than -10 dB across the band. The leakage to the other port of an LWA (Port 1 to Port 2) is less than -15 dB across the range. Due to the placement of a via wall that separates the two LWAs, the isolation between adjacent ports of the two LWAs (Port 1 and Port 2) is greater than 35 dB across the band.

IV. ON-CHIP 360–400-GHz TRANSCEIVER ARCHITECTURE

The architecture incorporating two dual-port integrated antennas with integrated 360–400-GHz transceivers is shown in Fig. 13. The two antennas interface with the transmit and receive pairs from the opposite end to sustain the operation, as depicted in Fig. 4. The chip is realized in a 65-nm bulk CMOS process.

In each transmitter chain, the LO frequency is injected at 60–67 GHz and then converted into the differential mode with an on-chip balun. The pad to the input of the three-stage PA has the peak matching efficiency of -2.85 dB and maintains the input reflection of less than -10 dB within the frequency band of operation. The balun needs to be designed to minimize amplitude and phase mismatches at the output across the frequency range. This preserves the performance of the frequency doubler and frequency tripler. In the designed balun, the amplitude mismatch is less than 0.25 dB, while the phase mismatch is less than 1.5° between 60 and 70 GHz. The differential signal is amplified by a three-stage power amplifier and fed to a frequency doubler followed by the frequency tripler. The chain generates output signals in the frequency range of 360–400 GHz that is fed into the leaky-waveguide antenna pair from the two ends (see Fig. 13).

On the receiver side, the output of the doubler in the LO chain is converted into a differential mode with an on-chip balun between 120 and 133 GHz. The differential LO drives
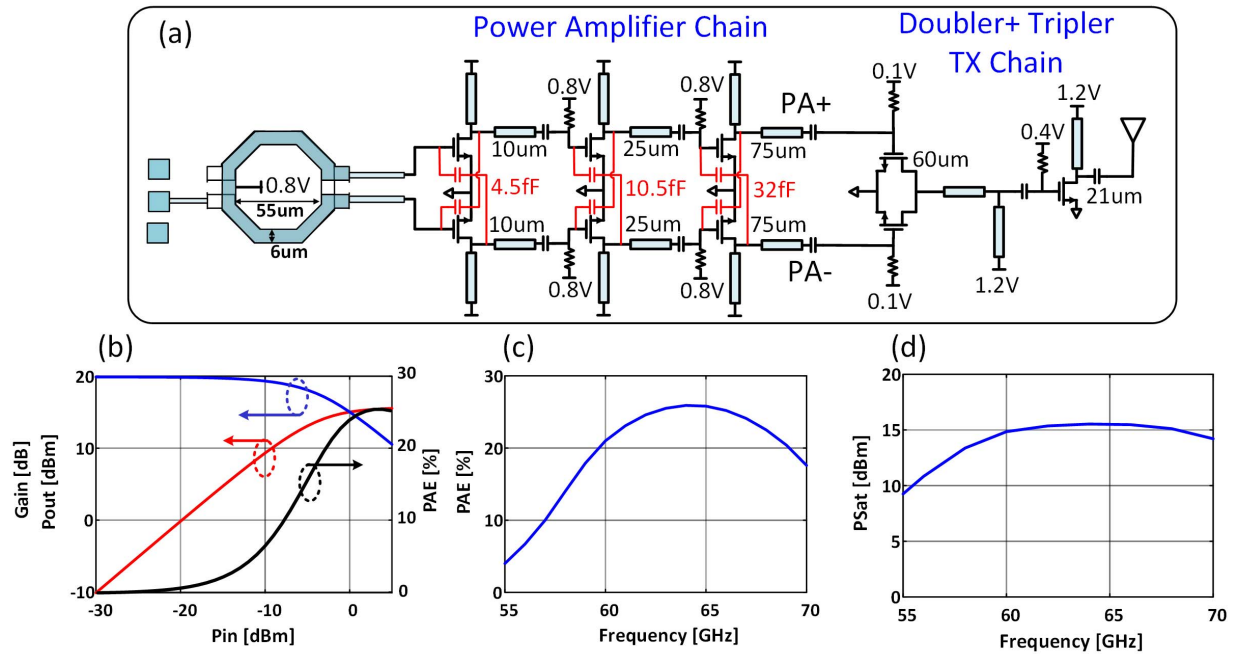
Fig. 14. Integrated THz transmitting chain. (a) Transmitting chain schematic including input balun, differential PA, frequency doubler, and frequency tripler. (b) PA large-signal performance at 65 GHz. (c) PA saturated output power versus frequency. (d) PAE versus frequency.

two separate triplers to create a differential drive between 360 and 400 GHz for the double-balanced passive mixers. The input signal from the antenna is also converted to a differential signal through a 360–400-GHz rat-race balun and down-converted into IF through the passive mixers. The IF is amplified on-chip with a broadband IF amplifier. The receiver chain consumes a total power of 163 mW, and the transmitter chain consumes a total dc power of 138 mW.

A. 60–67-GHz Power Amplifier

The PA amplifies the differential LO signal to drive the doubler [see Fig. 14(a)] [43], [44]. The PA schematic is shown in Fig. 14(a). The PA is based on a differential three-stage topology with transmission-line matching. In each stage of the PA, neutralization capacitors are utilized to neutralize the effect of the gate to drain capacitors. By placing these capacitors, the effective gate-to-drain capacitances can be reduced that leads to the enhancement of the reverse isolation gain and stability. The PA achieves a peak P_{sat} of 15.5 dBm and a peak power-added efficiency (PAE) of 25.9% [see Fig. 14(b)]. The PA achieves a 19.9 dB of small-signal gain at 65 GHz and maintains more than 22% PAE and more than 15 dBm output power across 60–67 GHz. In the designed three-stage PA, the transistors are sized 10, 25, and 75 μm in each branch correspondingly. The sizing of the transistors is chosen appropriately to provide enough power to saturate the following stages while accounting for both the inter-stage matching losses and optimal dc power consumption.

B. Frequency Multipliers

The differential output of PA is fed into the on-chip frequency doubler, biased in the cutoff region. As shown in Fig. 14(a), the fundamental signal is suppressed, and
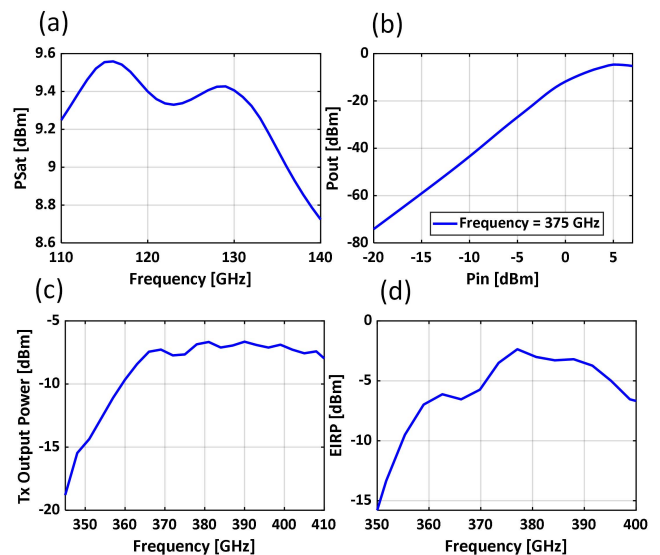

Fig. 15. Transmitting chain simulated performance. (a) Frequency doubler saturated power versus frequency. (b) Frequency tripler output power versus input power at output frequency of 375 GHz. (c) Transmitter chain output power versus frequency. (d) EIRP versus frequency of the Tx Chain.

the second harmonic (120–134 GHz) drives the succeeding frequency tripler to generate signals in the range of 360–400 GHz. As shown in Fig. 15(a), the frequency doubler has a simulated peak saturated power of 9.5 dBm across the band of interest. The generated power drives the frequency tripler into saturation [see Fig. 15(b)]. The tripler generates a peak power of −7.0 dBm at 375 GHz. The frequency doubler has the conversion efficiency of −7 dB, and the frequency tripler has the efficiency of −16 dB. The transmitter chain power across 360–400 GHz in Fig. 15 shows power generation capability of −9.5 to −7.2 dBm and effective-isotropic-radiated power (EIRP) of −6.7 to −2.7 dBm across
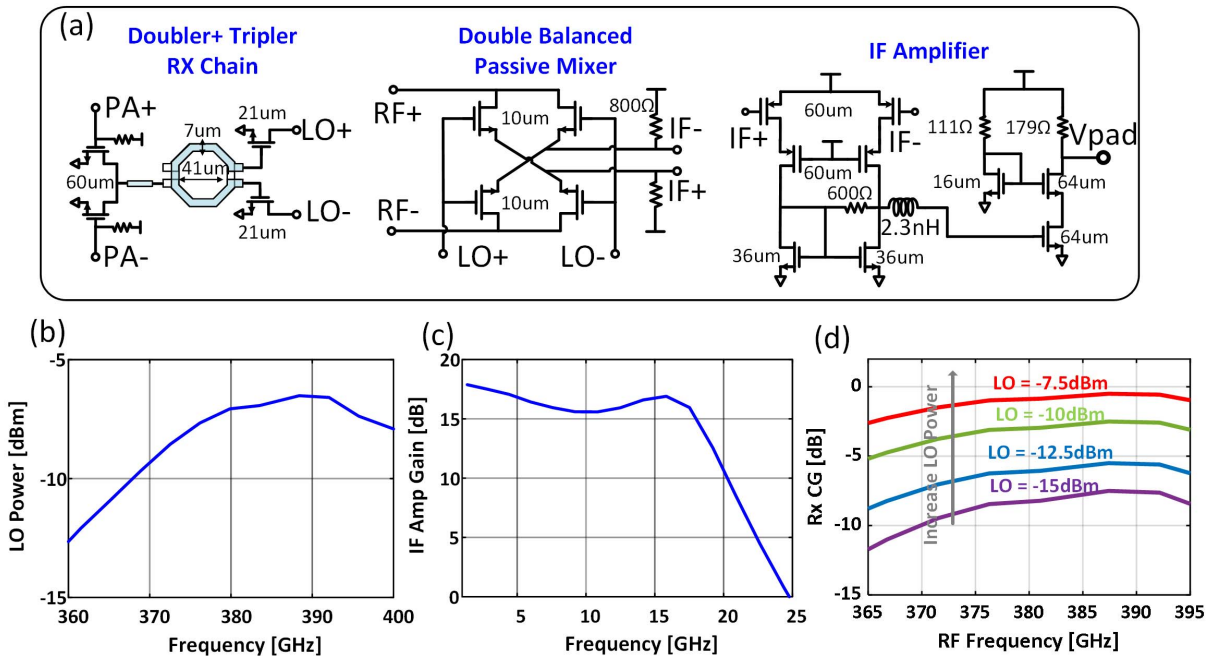
Fig. 16. Integrated THz receiver chain architecture across 360–400 GHz. (a) Receiver schematic including LO generation, mixing, and IF amplifier. (b) On-chip generated LO power versus frequency to drive the passive mixers. (c) IF amplifier gain versus frequency. (d) Rx conversion gain for LO frequency of 380 GHz for different LO power levels.

360–400-GHz range. The frequency tripler does not internally suppress the fundamental- and second-harmonic frequencies. The lower cutoff frequency of the LWA ensures that only the third-harmonic wave above 360 GHz is launched.

C. LO Path: Buffering and Frequency Multiplication

In the LO path, the input 60–67-GHz signal is amplified by the on-chip PA with the same topology as the one described in the transmitter path. The signal is then frequency-doubled, converted into a differential signal with a 120–135-GHz balun, and eventually injected into two on-chip frequency triplers, as shown in Fig. 16(a). The LO power generation across 360–400 GHz is shown in Fig. 16(b).

D. Double-Balanced Passive Mixer and If Amplifier

A double-balanced passive mixer is used for down-conversion. Due to the frequency of operation being higher than f_{max} of the device technology, the mixer interfaces directly with the antenna [45], [46]. The down-converted signal is amplified using an IF amplifier with a series peaking enhanced BW of 18 GHz and a gain of 18 dB [see Fig. 16(c)]. The receiver has a simulated conversion gain (excluding the antenna) of -2.5 to -0.5 dB while varying the THz frequency within 360–400-GHz range with the fixed LO frequency of 380 GHz, as shown in Fig. 16(d). In this figure, the LO power is varied at different power levels ranging from -15 to -7.5 dBm.

E. 120-GHz Balun and 360–400-GHz Rat-Race Balun

The balun in the LO path has a simulated loss of around 1–2 dB and a phase mismatch less than $5°$ within the frequency range of interest (see Fig. 17). The signal received

at the antenna is converted into a differential signal with an on-chip compact on-chip rat-race balun, as shown in Fig. 18. The dimensions are shown in the figure. The rat-race balun has a simulated output amplitude mismatch of less than 1 dB across 360–400 GHz and a differential phase mismatch of less than $6°$ across the frequency range.

F. Multi-Tone Detection

In a localization environment, the frequency content of signals spread between 360 and 400 GHz can be incident on the receiver at any given instant. To accommodate the large frequency range without being limited by the IF amplifier BW (18 GHz), the LO frequency can be chosen to create unique tones that are down-converted from the upper frequency range and the lower frequency range. As shown in Fig. 19, the LO frequency can be placed in the middle of the range (close to 380 GHz) with a slight offset that creates tones with an unequal and unique spacing of multiples of Δ_1 in the lower band and Δ_2 in the upper band. This leads to alternative placements of upper and lower band tones in the down-converted received spectrum. As can be seen, the higher band will form the odd tones, and the lower band will create the even-numbered tones, allowing the receiver to uniquely decode the incident spectrum.

V. MEASUREMENT RESULTS

The chip is fabricated in a 65-nm industry-standard CMOS process with f_{max} of 250 GHz. The chip occupies an area of 3 mm × 1 mm. The chip micro-graph is shown in Fig. 20, and the package is shown in Fig. 20. The performance of the on-chip antenna, the transmitter chain, and the receiver chain of the fabricated chip is characterized separately. For 1-D localization measurements, we use a single-chip
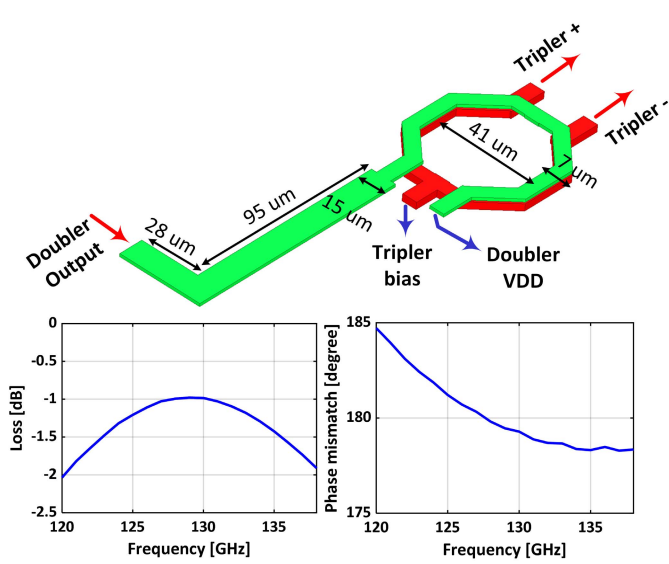
Fig. 17. On-chip balun across 120–133 GHz placed between the frequency doubler and differential tripler in the Rx Chain, and the corresponding simulated performance.
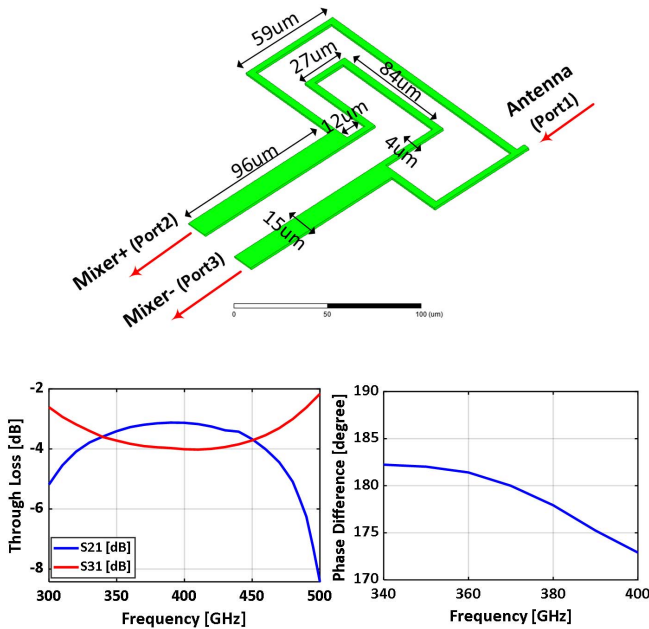

Fig. 18. On-chip compact rat-race balun across 360–400 GHz placed between the antenna and the mixer RF input, and its simulated performance.

system. We perform 2-D measurements with two orthogonal placed ICs.

A. Measurement Setup

To characterize the IC operating in transmitting (receiving) mode, an external broadband receiver (transmitter) chain placed on the rotational stage has been utilized. The measurement setup photograph is shown in Fig. 21. To characterize the transmitter chains in the IC [see Fig. 21(a)], we realize an external calibrated receiver chain consisting of Virginia Diodes signal generation module SGX WR9.0 along with WR4.3 frequency doubler and WR2.2 sub-harmonic mixer connected to the WR2.2 horn antenna. The down-converted IF
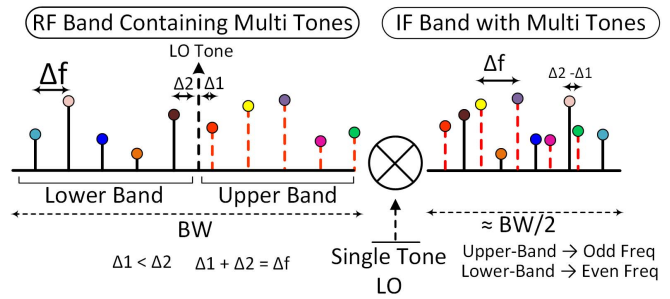

Fig. 19. Setting the LO frequency at the center of the received tones with a slight offset, the lower and the upper band tones can be uniquely decoded by the receiver.
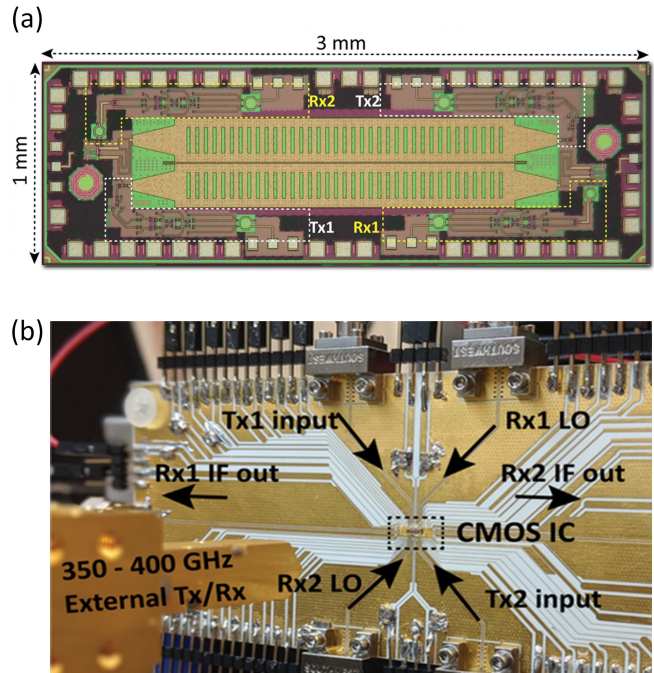

Fig. 20. THz Prism chip and packaged photograph. (a) Chip micrograph of the THz Prism occupying 3 mm^2. (b) Chip packaging and external connectors.

signal is then captured on a spectrum analyzer. To characterize the receiver chains of the IC [see Fig. 21(b)], we use a similar signal generation chain to synthesize the signal radiated onto the chip across 360–400 GHz.

B. Antenna Characterization

We measure the radiation patterns of CIW-based dual-port LWAs by enabling the on-chip transmitting chains. The input signal in the 60–67-GHz range is amplified by on-chip PAs and frequency multipliers to synthesize the output frequency in the 360–400-GHz range. For the two dual-port LWAs, the THz signal is injected from two opposite ports of the two LWAs through a co-design methodology [47], [48]. As shown in Fig. 22(a), injecting the signal from each end of the LWA allows one quadrant coverage due to the fast nature of the propagating fast wave within the CIW. Dual-port injections of the two separate LWAs, thereby, allow us to cover the entire ±40° range. The simulated pointing angles versus the measured pointing angles are shown in Fig. 22(b). These
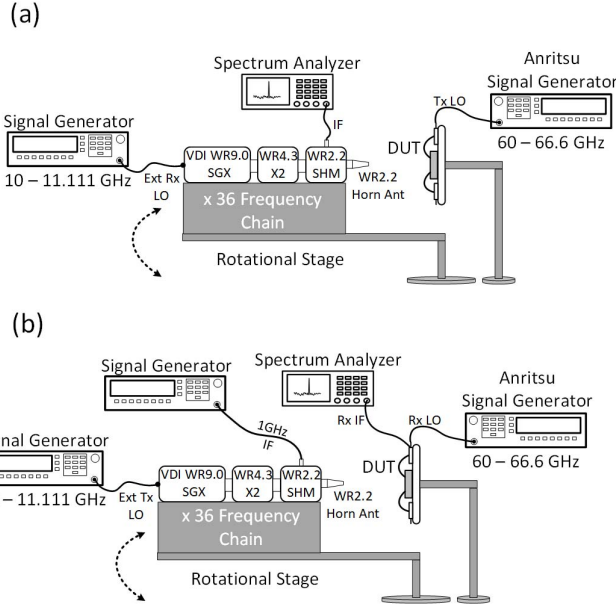
(a)

(b)

Fig. 21. THz transceiver characterization. (a) Far-field measurement setup of the on-chip transmitter. (b) Far-field measurement setup of the on-chip receiver.
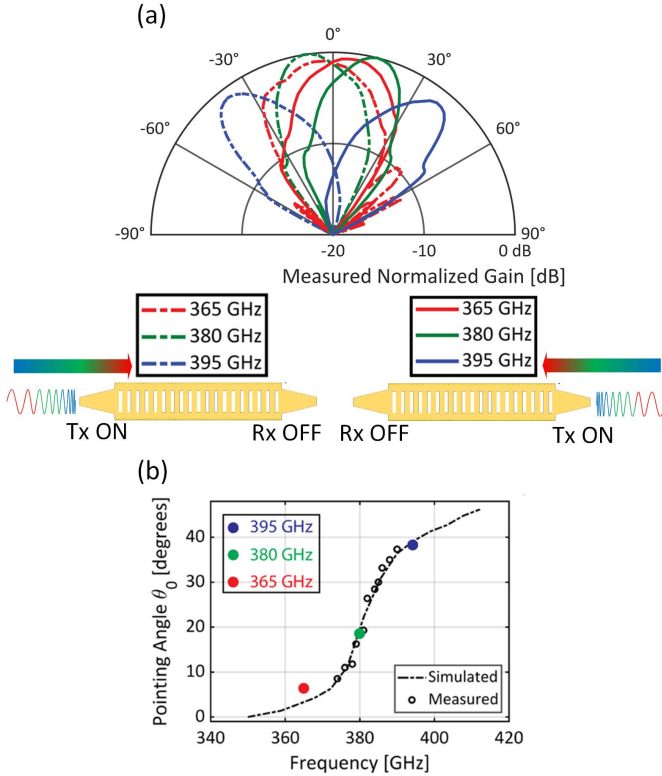
(a)

(b)

Fig. 22. Measured radiation characteristics. (a) Measured beam patterns across 360–400 GHz by enabling the two opposite ports of the two dual-port LWAs. (b) Measured (and simulated) beam maxima variation as the frequency varies between 360 and 400 GHz.

dynamic frequency-dependent radiation patterns serve as the basis vectors for the single-shot localization measurements.

C. Far-Field Transceiver Measurements

In this section, the antenna-coupled transmit and receive chains are characterized, as shown in Fig. 21.
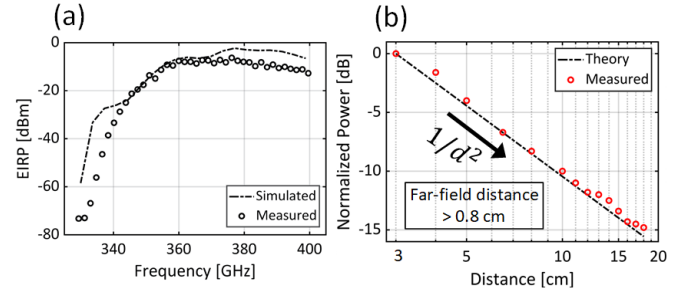
(a)

(b)

Fig. 23. Measured transmit performance. (a) Measured and simulated EIRP across 360–400 GHz. (b) Measured receive power against measurement distance showing the expected far-field $1/d^2$ dependence. The receiver starting placement is 3 cm, which is greater than 0.8 cm as the minimum far-field distance.

1) LWA Coupled Transmit Chain Characterization: The measurement results in Fig. 22(b) show that the pointing angle of the radiation pattern changes as a function of THz frequency. To calibrate the EIRP at each operating frequency, we scan the receiver chain across the 1-D angular dimension. EIRP is calculated based on the calibrated measured power at the antenna of the external receiver

$$\text{EIRP} = P_T G_T = \frac{P_R}{G_R \left(\dfrac{\lambda}{4\pi R}\right)^2} \tag{9}$$

where P_R is the calibrated received power at the external receiver, λ is the free-space wavelength at the frequency of operation, G_R is gain of the receiver horn antenna, and R is the distance between the chip and the external receiver chain.

The measured and simulated EIRP against frequency is shown in Fig. 23(a). A peak EIRP of -6.4 dBm is measured at the operating frequency of 378 GHz. As an extension to this measurement, the receiver is placed at varying distances in the far-field at the same frequency, and the received power is measured. As shown in Fig. 23(b), the measured power P_R falls with the measured distance, d as $1/d^2$, as expected. The minimum far-field distance, based on the aperture size of the radiating element, is 0.8 cm.

2) LWA Coupled Receiver Chain Characterization: To characterize the receiver mode of the THz Prism chip, the chip is irradiated with calibrated THz power, as shown in Fig. 21(b). The power incident on the LWA on-chip is measured as follows:

$$P_{\text{Rx,ant}}\big|_{\text{dBm}} = P_{\text{Tx}}\big|_{\text{dBm}} + G_{\text{Tx}}\big|_{\text{dB}} - L_{\text{path}}\big|_{\text{dB}} + D_{\text{Rx,ant}}\big|_{\text{dB}} \tag{10}$$

where P_{Tx} is the external total radiated power, G_{Tx} is the external horn antenna gain, L_{path} is the path loss, and $D_{\text{Rx,ant}}$ is the on-chip antenna directivity. The directivity is calculated from the measured radiation patterns in Fig. 22. The on-chip THz receiver chain conversion gain can, therefore, be calculated as follows:

$$R_{\text{CG}} = P_{\text{IF,out}}\big|_{\text{dBm}} - P_{\text{Rx,ant}}\big|_{\text{dBm}}. \tag{11}$$

Since the antenna is embedded into the receiver, we estimate the Rx noise figure by measuring the noise spectrum at the
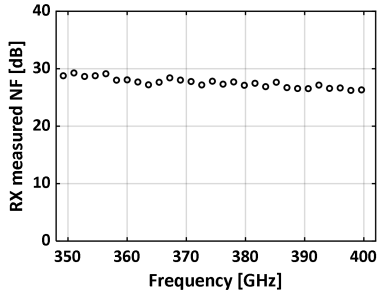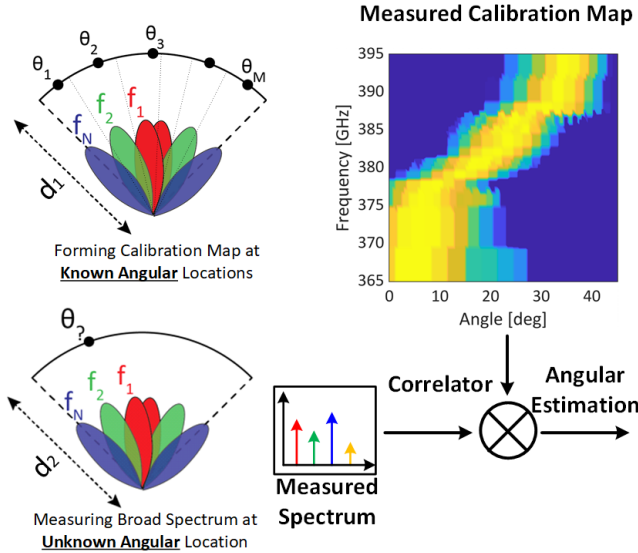
Fig. 24. Measured on-chip receiver noise figure.

Fig. 25. 1-D localization methodology with correlation of the measured spectrum against the spectrum-to-angle calibration map.
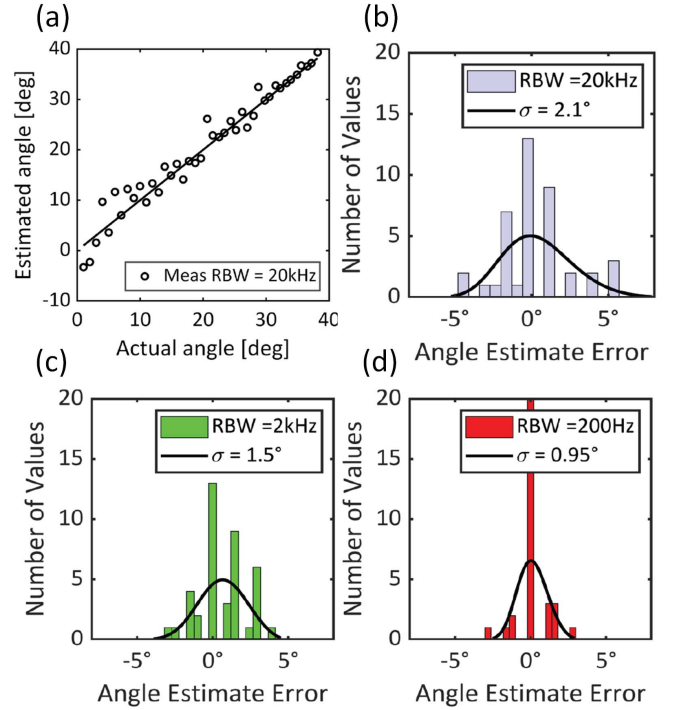

Fig. 26. Measured angular localization in 1-D. (a) Measured versus actual angular locations for resolution BW of 20 kHz. Measured histogram of errors and error variance for various resolution BWs: (b) 20 kHz, (c) 2 kHz, and (d) 200 Hz.

output of the IF. In the noise figure measurement, the noise spectrum of the Rx ($P_{n,\text{out}}$) was measured with a resolution BW of 200 Hz. The NF of the receiver chain was then estimated as

$$\text{NF} = P_{n,\text{out}}\big|_{\text{dBm}} - 10\log_{10}(\text{BW}) - (-174\ \text{dBm/Hz}) - R_{\text{CG}}.$$
$$(12)$$

The measured noise figure is shown in Fig. 24.

D. Single-Shot 1-D Localization

Here, we describe the detailed 1-D single-shot localization procedure and the algorithm. As the first step, we obtain a calibration map of spectral dispersion over space between 360 and 400 GHz with a 1.5-GHz step, as illustrated in Fig. 25. Once the map is obtained, we test the algorithm by placing a receiver at 40 different random locations placed at different distances comparing to the calibration map (6 cm comparing to 4 cm). The angular localization is obtained by correlating the measured spectrum with the calibration map, as shown in Fig. 25. A normalized cross correlation removes the dependency on absolute power. The information is embedded in the relative contributions of the spectral components and, therefore, allows angular localization across various distances. Environmental variations (such as temperature and humidity) can change the overall absorption across the band, but their

effect in modifying the spectral shape is expected to be minimal. However, this can also be mitigated with infrequent calibrations as necessary.

It is to be noted that the variation of the distance of the receiver does not affect the calibration map, and therefore, the angular localization procedure, in principle, is not affected by the Tx–Rx distance. Since the received power is reduced with longer distances, error variance increases for the same measurement time. Fig. 26(a) shows the measured angular positions compared against actual receiver locations when the resolution BW is set at 20 kHz. As expected, increasing the measurement time or equivalently decreasing the resolution BW enhances localization accuracy, as shown in Fig. 26(b)–(d). As the resolution BW reduces from 20 kHz (50 μs) to 200 Hz (5 ms), the error variance decreases from 2.1° to 0.95°. The error variance against resolution BW is shown in Fig. 27.

E. Single-Shot 1-D Chip-to-Chip Localization

As an extension to the aforementioned 1-D localization measurement using an external receiver chain, we show chip-to-chip localization enabling the transmitter on one chip and the receiver on the other. In this measurement, as shown in Fig. 28, the transmitter emits frequencies between 360 and 400 GHz. The received power by the Rx chip placed 2 cm away, as it slides along the axis, is shown in Fig. 28. As both the transmit and receive patterns are spectrally dependent, the net received power is a resultant convolution of both patterns. As shown in Fig. 28, the measured power peaks at various offsets depending on the frequency. As an example, for
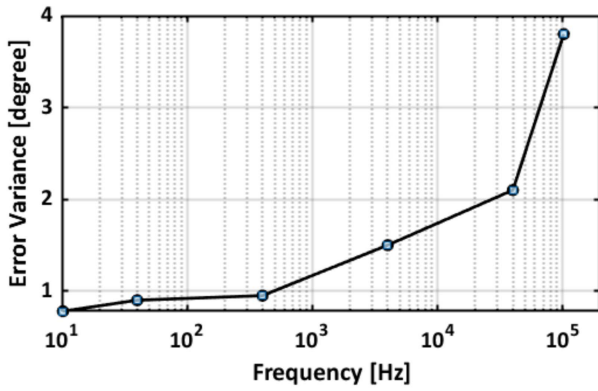
Fig. 27. Variation of localization error variance for 1-D measurements as a function of resolution BW or measurement time.
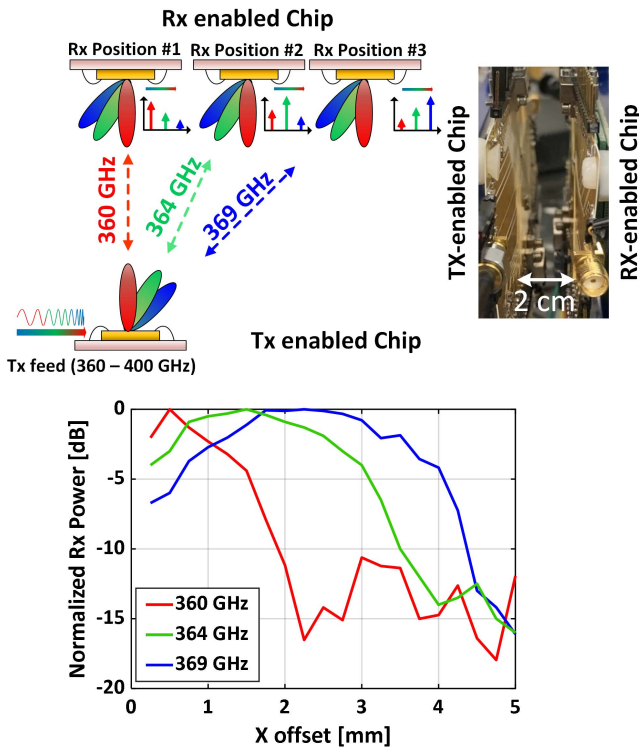

Fig. 28. Chip-to-chip angular localization in 1-D and measured power for various offsets at the receiver chip.

a frequency of 369 GHz, the peak shifts to a 2.2-mm offset that corresponds to an angular shift of 10°. Based on this approach, we can detect the angle of arrival when the clients move across the *X*-direction. There is also a possibility to estimate the orientation of the client through the analysis of the spectral width. Rotation of the client can create spectral broadening or narrowing that can be deciphered to estimate the client orientation [28].

F. Simultaneous Transmitter and Receiver Operations

The system architecture is designed to allow for simultaneous transmitting and receiving operations. This simultaneous operation can be operated in three different fashions, namely:
1) Tx and Rx operations from two adjacent on-chip LWAs;
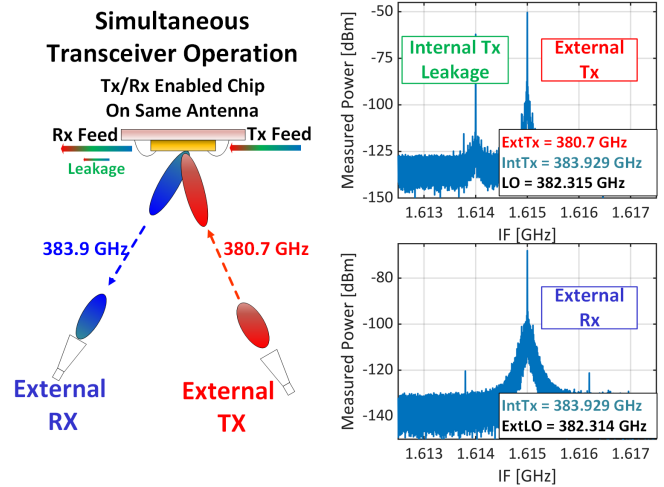2) Tx and Rx operations from the same on-chip LWA; and

Fig. 29. Full-duplex operation where the chip operates simultaneously in the transmit and receive modes utilizing single LWA.

3) two Tx and two Rx complete the operation from both on-chip LWAs. In Fig. 29, the full-duplex transceiver operation is shown when Tx and Rx are both turned on simultaneously on the same on-chip LWA. When Tx transmits to the external Rx (which is located in the one half-quadrant) and the measured spectrum is shown, an external Tx located in the half-quadrant transmits to the same on-chip LWA, and the received spectrum is also shown in Fig. 29.

G. Single-Shot 2-D Localization

Extending on the unique spectrum-to-space mapping for 1-D localization, we perform 2-D angular localization with two orthogonally placed ICs (see Fig. 30). To create a unique map, we add a slight frequency shift of 1 kHz between the transmitting frequency sets from Tx1 and Tx2. Such a small-frequency offset does not change the radiation patterns of these chips.

In a manner similar to the 1-D calibration map Fig. 25, we create an initial 2-D calibration map of the spectrum against angular locations in the 2-D space. The spectrum at any receiver location is the combination of the received signal radiated from the two orthogonally placed chips [see Fig. 30(a)]. For localization measurements, we program a transitional stage to place the receiver at 80 random locations. We estimate the location based on the correlation of the measured spectrum and the calibration map. This measurement is done with a resolution BW of 20 Hz.

The measured histogram of the error is shown in Fig. 30(b). The measured error variance is 1.9° and 1.95° at θ and ϕ, as shown in the figure. The packaged two orthogonally placed chips are shown in Fig. 31. The board is tilted by 45° to capture both horizontal and vertical polarizations with a single linearly polarized receiver.

In this work, while we demonstrated the localization principle through a C.W. sweep across 360–400 GHz, in principle, this can also be established with the generation and detection of broadband pulses. In such a scenario, the net localization time will be a combination of the Rx acquisition time and the Tx broadband spectrum synthesis time. If the total power of
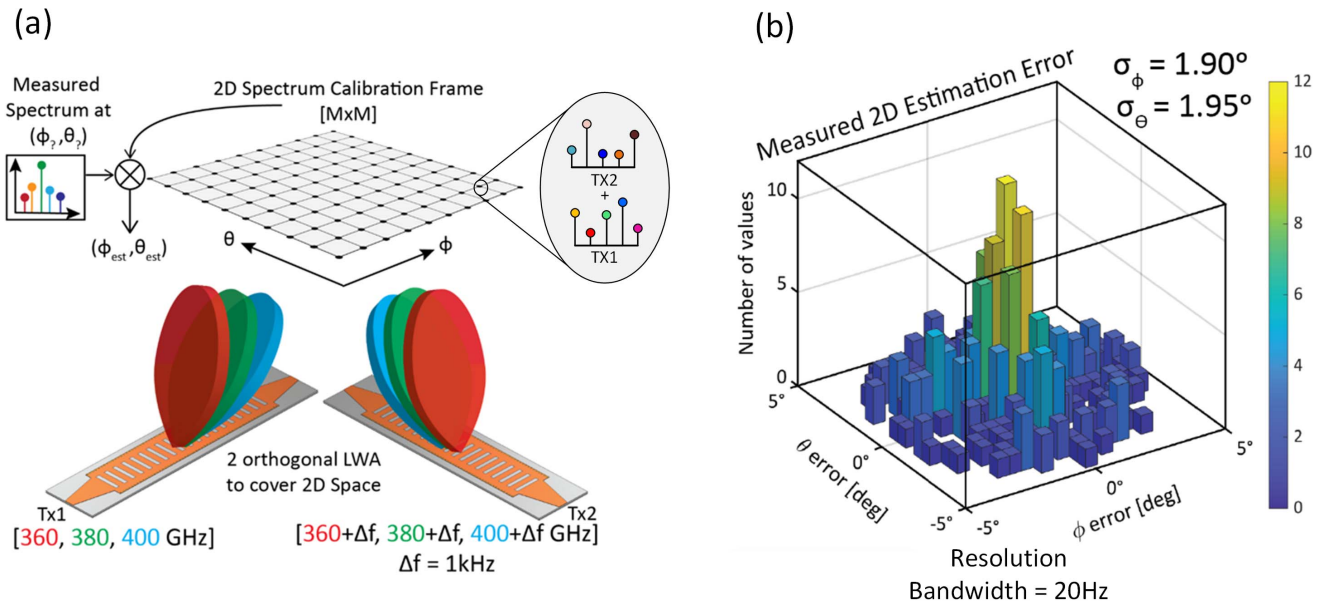
Fig. 30.   2-D localization. (a) Unique 2-D spectrum-to-space mapping with two orthogonally placed THz Prism chips. (b) Measured histogram of 2-D localization error and error variance for a resolution BW of 20 Hz.

TABLE I
COMPARISON WITH STATE-OF-THE-ART THz POWER GENERATION SOURCES

| Metrics	This work	[31]	[28]	[49]	[50]
Architecture	Tx/Rx + Onchip Antenna	Tx/Rx Dual off-chip ZBD + Dual off-chip LWA + Ext AMC	THz-TDS with fiber coupled photoconductive antennas as source	Tx/Rx FMCW comb radar with 5 on-chip multimode SIW antenna	Tx/Rx with On-chip Patch antenna
Antenna Type	Periodic LWA	Uniform Leaky-Wave Waveguide	Uniform LWA (Parallel plate Waveguide)	Multi-mode SIW Antenna	Differential Patch Antenna
Frequency Range [GHz]	360 - 400	330 - 490	150 - 750	220-320	300-375
Prad per Unit [dBm]	-10.9	-5 (off-chip active X-Chain)	N/A	0.6	3
Rx Noise Figure [dB]	26.2 (DSB avg)	N/A	N/A	22.2 DSB(min)	31.5 DSB avg (19.75 min)
Beam Coverage [°]	-40 to +40	-51 to +51	+10 to +80	N/A	N/A
DoA Accuracy [°]	+/- 0.95 (1D RBW = 200Hz) +/- 1.9 (2D RBW = 20Hz)	+/- 5	+/- 5	N/A	N/A
DC Power per Tx/Rx	Tx 138mW Rx 163mW	N/A(off-chip)	N/A(off-chip)	840 mW total	Tx 568mW Rx 751mW
Area [mm²]	3	N/A	N/A	5	2.85
Technology	65-nm CMOS	GaAs Schottky barrier ZBD with waveguide components	Off-the-shelf THz spectrometer components	65-nmos CMOS	130-nm SiGe
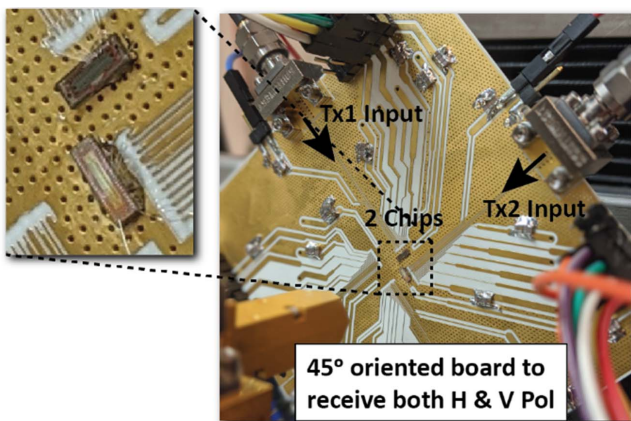
Fig. 31.   Chip packaging with two orthogonally placed THz Prism ICs for 2-D localization.

the Tx is instantaneously spread over the broadband spectrum (such as in a pulse), the integration time at the Rx needs to increase to maintain the desired SNR. This will overall keep the acquisition time approximately similar in both cases. On the Tx side, however, broadband pulse generation can be achieved in a more rapid fashion than a typical C.W. sweep that is limited by a PLL settling time. Collectively, instantaneous broadband signal processing is expected to allow a reduction of localization time.

The comparison with state-of-the-art THz localization and radar is presented in Table I. The chip presents, for the first time, a chip-integrated waveguide and LWA at THz on-chip capable of one-shot angular localization with integrated THz transceivers.

VI. CONCLUSION

In this work, we demonstrate a spectrum-to-space mapping principle for the simultaneous localization of multiple wireless nodes in 2-D angular space in a single-shot fashion. This is achieved with CIW-based LWAs that emit spectrally dependent radiation patterns. With the integrated 360–400-GHz transceivers interfacing with two dual-port LWAs, we cover $\pm40°$ of the radiation maxima. We demonstrate 1-D localization with $1°$ accuracy with a 200-Hz BW. We also demonstrate 2-D localization with less than $2°$ of error variance at 20-Hz-resolution BW. The ability to realize high-resolution localization in 2-D space in a single-shot fashion makes this highly attractive for wireless node localization, wireless link discovery, and beam-optimization methods.

REFERENCES

[1] T. S. Rappaport *et al.*, "Wireless communications and applications above 100 GHz: Opportunities and challenges for 6G and beyond," *IEEE Access*, vol. 7, pp. 78729–78757, 2019.

[2] K. Sengupta, T. Nagatsuma, and D. M. Mittleman, "Terahertz integrated electronic and hybrid electronic-photonic systems," *Nature Electron.*, vol. 1, pp. 622–635, Dec. 2018.

[3] K. Sengupta and A. Hajimiri, "A 0.28 THz power-generation and beam-steering array in CMOS based on distributed active radiators," *IEEE J. Solid-State Circuits*, vol. 47, no. 12, pp. 3013–3031, Dec. 2012.

[4] K. Sengupta, "Integrated circuits for terahertz communication beyond 100 GHz: Are we there yet?" in *Proc. IEEE Int. Conf. Commun. Workshops (ICC Workshops)*, May 2019, pp. 1–6.

[5] X. Wu, H. Lu, and K. Sengupta, "Programmable terahertz chip-scale sensing interface with direct digital reconfiguration at sub-wavelength scales," *Nature Commun.*, vol. 10, no. 1, pp. 1–13, Dec. 2019.

[6] Y. Niu, Y. Li, D. Jin, L. Su, and A. V. Vasilakos, "A survey of millimeter wave communications (mmWave) for 5G: Opportunities and challenges," *Wireless Netw.*, vol. 21, no. 8, pp. 2657–2676, 2015.

[7] X. Lu, S. Venkatesh, and H. Saeidi, "A review on applications of integrated terahertz systems," *China Commun.*, vol. 18, no. 5, pp. 175–201, May 2021.

[8] S. Venkatesh, X. Lu, B. Tang, and K. Sengupta, "Secure space-time modulated millimeter-wave wireless links that are resilient against distributed eavesdropper attacks," *Nature Electron*, to be published.

[9] C. R. Chappidi and K. Sengupta, "Frequency reconfigurable mm-wave power amplifier with active impedance synthesis in an asymmetrical non-isolated combiner: Analysis and design," *IEEE J. Solid-State Circuits*, vol. 52, no. 8, pp. 1990–2008, Aug. 2017.

[10] K. Sengupta, X. Lu, S. Venkatesh, and B. Tang, "Physically secure sub-THz wireless links," in *Proc. IEEE Int. Conf. Commun. Workshops (ICC Workshops)*, Jun. 2020, pp. 1–7.

[11] E. Naviasky, L. Iotti, G. LaCaille, B. Nikolic, E. Alon, and A. Niknejad, "14.1 A 71-to-86 GHz packaged 16-element by 16-beam multi-user beamforming integrated receiver in 28 nm CMOS," in *IEEE Int. Solid-State Circuits Conf. (ISSCC) Dig. Tech. Papers*, Feb. 2021, pp. 218–220.

[12] H.-J. Song, "Terahertz wireless communications: Recent developments including a prototype system for short-range data downloading," *IEEE Microw. Mag.*, vol. 22, no. 5, pp. 88–99, May 2021.

[13] A. Mostajeran *et al.*, "A high-resolution 220-GHz ultra-wideband fully integrated ISAR imaging system," *IEEE Trans. Microw. Theory Techn.*, vol. 67, no. 1, pp. 429–442, Jan. 2019.

[14] Y.-N.-R. Li, B. Gao, X. Zhang, and K. Huang, "Beam management in millimeter-wave communications for 5G and beyond," *IEEE Access*, vol. 8, pp. 13282–13293, 2020.

[15] H. Saeidi, S. Venkatesh, C. R. Chappidi, T. Sharma, C. Zhu, and K. Sengupta, "29.9 A 4×4 distributed multi-layer oscillator network for harmonic injection and THz beamforming with 14 dBm EIRP at 416 GHz in a lensless 65 nm CMOS IC," in *IEEE Int. Solid-State Circuits Conf. (ISSCC) Dig. Tech. Papers*, Feb. 2020, pp. 256–258.

[16] S. Razavian, M. Hosseini, Y. Mehta, and A. Babakhani, "Terahertz channel characterization using a broadband frequency comb radiator in 130-nm SiGe BiCMOS," *IEEE Trans. THz Sci. Technol.*, vol. 11, no. 3, pp. 269–276, May 2021.

[17] S. Venkatesh, X. Lu, H. Saeidi, and K. Sengupta, "A high-speed programmable and scalable terahertz holographic metasurface based on tiled CMOS chips," *Nature Electron.*, vol. 3, no. 12, pp. 785–793, Dec. 2020.

[18] S. Razavian and A. Babakhani, "A THz pulse radiator based on PIN diode reverse recovery," in *Proc. IEEE BiCMOS Compound semiconductor Integr. Circuits Technol. Symp. (BCICTS)*, Nov. 2019, pp. 1–4.

[19] H. Afzal, R. Abedi, R. Kananizadeh, P. Heydari, and O. Momeni, "An mm-wave scalable PLL-coupled array for phased-array applications in 65-nm CMOS," *IEEE Trans. Microw. Theory Techn.*, vol. 69, no. 2, pp. 1439–1452, Feb. 2021.

[20] S. Venkatesh, D. Shrekenhamer, W. Xu, S. Sonkusale, W. Padilla, and D. Schurig, "Interferometric direction finding with a metamaterial detector," *Appl. Phys. Lett.*, vol. 103, no. 25, Dec. 2013, Art. no. 254103.

[21] Y. Yang, O. D. Gurbuz, and G. M. Rebeiz, "An eight-element 370–410-GHz phased-array transmitter in 45-nm CMOS SOI with peak EIRP of 8–8.5 dBm," *IEEE Trans. Microw. Theory Techn.*, vol. 64, no. 12, pp. 4241–4249, Dec. 2016.

[22] Y. Tousi and E. Afshari, "A high-power and scalable 2-D phased array for terahertz CMOS integrated systems," *IEEE J. Solid-State Circuits*, vol. 50, no. 2, pp. 597–609, Feb. 2015.

[23] H. Jalili and O. Momeni, "A 0.34-THz wideband wide-angle 2-D steering phased array in 0.13-μm SiGe BiCMOS," *IEEE J. Solid-State Circuits*, vol. 54, no. 9, pp. 2449–2461, 2019.

[24] U. R. Pfeiffer *et al.*, "A 0.53 THz reconfigurable source module with up to 1 mW radiated power for diffuse illumination in terahertz imaging applications," *IEEE J. Solid-State Circuits*, vol. 49, no. 12, pp. 2938–2950, Dec. 2014.

[25] H. Jalili and O. Momeni, "23.2 A 436-to-467GHz lens-integrated reconfigurable radiating source with continuous 2D steering and multi-beam operations in 65 nm CMOS," in *IEEE Int. Solid-State Circuits Conf. (ISSCC) Dig. Tech. Papers*, vol. 64, Feb. 2021, pp. 326–328.

[26] R. Jain, P. Hillger, J. Grzyb, and U. R. Pfeiffer, "29.1 A 0.42 THz 9.2 dBm 64-pixel source-array SoC with spatial modulation diversity for computational terahertz imaging," in *IEEE Int. Solid-State Circuits Conf. (ISSCC) Dig. Tech. Papers*, Mar. 2020, pp. 440–442.

[27] H. Hassanieh, O. Abari, M. Rodriguez, M. Abdelghany, D. Katabi, and P. Indyk, "Fast millimeter wave beam alignment," in *Proc. Conf. ACM Special Interest Group Data Commun.*, New York, NY, USA, Aug. 2018, pp. 432–445, doi: 10.1145/3230543.3230581.

[28] Y. Ghasempour, R. Shrestha, A. Charous, E. Knightly, and D. M. Mittleman, "Single-shot link discovery for terahertz wireless networks," *Nature Commun.*, vol. 11, no. 1, pp. 1–6, Dec. 2020.

[29] K. Sengupta and A. Hajimiri, "Designing optimal surface currents for efficient on-chip mm-wave radiators with active circuitry," *IEEE Trans. Microw. Theory Techn.*, vol. 64, no. 7, pp. 1976–1988, Jul. 2016.

[30] H. Saeidi, S. Venkatesh, X. Lu, and K. Sengupta, "22.1 THz prism: One-shot simultaneous multi-node angular localization using spectrum-to-space mapping with 360-to-400 GHz broadband transceiver and dual-port integrated leaky-wave antennas," in *IEEE Int. Solid-State Circuits Conf. (ISSCC) Dig. Tech. Papers*, Feb. 2021, pp. 314–316.

[31] H. Matsumoto, I. Watanabe, A. Kasamatsu, and Y. Monnai, "Integrated terahertz radar based on leaky-wave coherence tomography," *Nature Electron.*, vol. 3, no. 2, pp. 122–129, Feb. 2020.

[32] F. Xu, K. Wu, and X. Zhang, "Periodic leaky-wave antenna for millimeter wave applications based on substrate integrated waveguide," *IEEE Trans. Antennas Propag.*, vol. 58, no. 2, pp. 340–347, Feb. 2010.

[33] J. Liu, D. R. Jackson, and Y. Long, "Modal analysis of dielectric-filled rectangular waveguide with transverse slots," *IEEE Trans. Antennas Propag.*, vol. 59, no. 9, pp. 3194–3203, Sep. 2011.

[34] D.-F. Guan *et al.*, "Scanning rate enhancement of leaky-wave antennas using slow-wave substrate integrated waveguide structure," *IEEE Trans. Antennas Propag.*, vol. 66, no. 7, pp. 3747–3751, Jul. 2018.

[35] J. Liu, D. R. Jackson, and Y. Long, "Substrate integrated waveguide (SIW) leaky-wave antenna with transverse slots," *IEEE Trans. Antennas Propag.*, vol. 60, no. 1, pp. 20–29, Jan. 2012.

[36] J.-D. Park and A. M. Niknejad, "Y-band on-chip dual half-width leaky-wave antenna in a nanoscale CMOS process," *IEEE Antennas Wireless Propag. Lett.*, vol. 12, pp. 1476–1479, 2013.

[37] R. Hyneman, "Closely-spaced transverse slots in rectangular waveguide," *IRE Trans. Antennas Propag.*, vol. 7, no. 4, pp. 335–342, Oct. 1959.

[38] J. N. Hines, V. H. Rumsey, and C. H. Walter, "Traveling-wave slot antennas," *Proc. IRE*, vol. 41, no. 11, pp. 1624–1631, Nov. 1953.

[39] F. Xu and K. Wu, "Guided-wave and leakage characteristics of substrate integrated waveguide," *IEEE Trans. Microw. Theory Techn.*, vol. 53, no. 1, pp. 66–73, Jan. 2005.

[40] Q. Song, S. Campione, O. Boyraz, and F. Capolino, "Silicon-based optical leaky wave antenna with narrow beam radiation," *Opt. Exp.*, vol. 19, no. 9, pp. 8735–8749, 2011.

[41] Y. D. Dong and T. Itoh, "Composite right/left-handed substrate integrated waveguide and half mode substrate integrated waveguide leaky-wave structures," *IEEE Trans. Antennas Propag.*, vol. 59, no. 3, pp. 767–775, Mar. 2011.

[42] Y. Shang, Y. Yu, P. Li, Y. Liang, and C. Yang, "A 280 GHz CMOS on-chip composite right/left handed transmission line based leaky wave antenna with broadside radiation," in *IEEE MTT-S Int. Microw. Symp. Dig.*, Jun. 2014, pp. 1–3.

[43] X. Lu, S. Venkatesh, B. Tang, and K. Sengupta, "Space-time modulated 71-to-76 GHz mm-wave transmitter array for physically secure directional wireless links," in *IEEE Int. Solid-State Circuits Conf. (ISSCC) Dig. Tech. Papers*, Feb. 2020, pp. 86–88.

[44] P. M. Farahabadi and K. Moez, "A 60-GHz dual-mode distributed active transformer power amplifier in 65-nm CMOS," *IEEE Trans. Very Large Scale Integr. (VLSI) Syst.*, vol. 24, no. 5, pp. 1909–1916, May 2016.

[45] H.-J. Song, J.-Y. Kim, K. Ajito, N. Kukutsu, and M. Yaita, "50-Gb/s direct conversion QPSK modulator and demodulator MMICs for terahertz communications at 300 GHz," *IEEE Trans. Microw. Theory Techn.*, vol. 62, no. 3, pp. 600–609, Mar. 2014.

[46] J.-D. Park, S. Kang, and A. M. Niknejad, "A 0.38 THz fully integrated transceiver utilizing a quadrature push-push harmonic circuitry in SiGe BiCMOS," *IEEE J. Solid-State Circuits*, vol. 47, no. 10, pp. 2344–2354, Oct. 2012.

[47] X. Lu, C. Reddy Chappidi, X. Wu, and K. Sengupta, "Antenna pre-processing and element-pattern shaping for multi-band mmWave arrays: Multi-port receivers and antennas," *IEEE J. Solid-State Circuits*, vol. 55, no. 6, pp. 1455–1470, Jun. 2020.

[48] C. Reddy Chappidi, X. Lu, X. Wu, and K. Sengupta, "Antenna pre-processing and element-pattern shaping for multi-band mmWave arrays: Multi-port transmitters and antennas," *IEEE J. Solid-State Circuits*, vol. 55, no. 6, pp. 1441–1454, Jun. 2020.

[49] X. Yi, C. Wang, M. Lu, J. Wang, J. Grajal, and R. Han, "4.8 A terahertz FMCW comb radar in 65 nm CMOS with 100GHz bandwidth," in *IEEE Int. Solid-State Circuits Conf. (ISSCC) Dig. Tech. Papers*, Feb. 2020, pp. 90–92.

[50] J. Al-Eryani, H. Knapp, J. Kammerer, K. Aufinger, H. Li, and L. Maurer, "Fully integrated single-chip 305–375-GHz transceiver with on-chip antennas in SiGe BiCMOS," *IEEE Trans. THz Sci. Technol.*, vol. 8, no. 3, pp. 329–339, May 2018.

Hooman Saeidi (Graduate Student Member, IEEE) received the bachelor's degree in electrical engineering from the Sharif University of Technology, Tehran, Iran, in 2017. He is currently pursuing the master's degree with Princeton University, Princeton, NJ, USA.

His research interests include electromagnetics, mm-wave, and THz circuits and integrated circuits for high data rate communication systems.

Suresh Venkatesh (Member, IEEE) received the M.S. degree in electrical and computer engineering from North Carolina State University, Raleigh, NC, USA, in 2010, and the Ph.D. degree in electrical and computer engineering from The University of Utah, Salt Lake City, UT, USA, in 2017, under the guidance of Prof. David Schurig.

He was a Research Project Assistant with the Molecular Astronomy Laboratory, Raman Research Institute, Bengaluru, India, from 2007 to 2008, where he worked on a millimeter-wave radio telescope. He is currently a Post-Doctoral Researcher with the Integrated Micro-Systems Research Laboratory, Electrical and Computer Engineering Department, Princeton University, Princeton, NJ, USA. He has authored/coauthored more than 40 journal and conference publications. His research interests are in electromagnetics, metamaterials, antenna design, integrated circuits, computational imaging, and transformation optics design.

Dr. Venkatesh is also an Affiliate Member of the MTT-23 Wireless Communication Committee and is also serving as the IEEE MTTS YP Region 1-6 Coordinator. He also serves as a Committee Member of the Climate and Inclusion Committee, Electrical and Computer Engineering Department, Princeton University. He was a recipient of the 2021 Mistletoe Research Fellowship from the Momental Foundation. His Ph.D. dissertation received the ECE Outstanding Dissertation Award in 2016.

Xuyang Lu (Member, IEEE) received the B.S. degree in electrical engineering from Rice University, Houston, TX, USA, in 2014, and the M.A. and Ph.D. degrees in electrical engineering from Princeton University, Princeton, NJ, USA, in 2016 and 2020, respectively.

He joined the University of Michigan–Shanghai Jiao Tong University Joint Institute, Shanghai Jiao Tong University, Shanghai, China, in 2021, as a Faculty Member. His research interests include high-speed programmable RF and mm-Wave integrated systems, integrated terahertz systems, integrated photonics, on-chip antenna optimization, and machine learning in analog circuit design.

Kaushik Sengupta (Senior Member, IEEE) received the B.Tech. and M.Tech. degrees in electronics and electrical communication engineering from IIT Kharagpur, Kharagpur, India, in 2007, and the M.S. and Ph.D. degrees in electrical engineering from the California Institute of Technology (Caltech), Pasadena, CA, USA, in 2008 and 2012, respectively.

He performed research at the University of Southern California, Los Angeles, CA, USA, and the Massachusetts Institute of Technology, Cambridge, MA, USA, in 2005 and 2006, respectively, where he was involved in nonlinear integrated systems for high-purity signal generation and low-power RF identification tags. He joined the Department of Electrical Engineering, Princeton University, Princeton, NJ, USA, as a Faculty Member, in 2013, where he is currently an Associate Professor and the Director of Graduate Studies. His current research interests include high-frequency ICs, electromagnetics, and optics for various applications in sensing, imaging, and high-speed communication.

Dr. Sengupta is also a member of the MTT-4 Committee on Terahertz Technology. He was a recipient of the Outstanding Young Engineer Award from IEEE TRANSACTIONS ON MICROWAVE THEORY AND TECHNIQUES in 2021. He received the DARPA Young Faculty Award in 2018, the Bell Labs Prize in 2017, the Young Investigator Program Award from the Office of Naval Research in 2017, the E. Lawrence Keys, Jr. Emerson Electric Co. Junior Faculty Award from the Princeton School of Engineering and Applied Science in 2018, and the Excellence in Teaching Award in 2018 nominated by the Undergraduate and Graduate Student Council in the Princeton School of Engineering and Applied Science. He was a recipient of the Charles Wilts Prize in 2013 from the Department of Electrical Engineering, Caltech, for the best Ph.D. thesis, the Caltech Institute Fellowship, the Prime Minister Gold Medal Award of IIT in 2007, and the Inaugural Young Alumni Achievement Award from IIT Kharagpur. He was a co-recipient of the IEEE RFIC Symposium Best Student Paper Award in 2012, multiple best student paper awards in IEEE International Microwave Symposium (IMS), and the 2015 Microwave Prize from the IEEE Microwave Theory and Techniques Society. He also serves as the Chair of Emerging Technologies for IEEE Custom Integrated Circuits Conference (CICC) and the Steering Committee of the IEEE IMS. He has served as a Distinguished Lecturer of the IEEE Solid-State Circuits Society from 2019 to 2020. He is also serving as a Distinguished Lecturer of the IEEE Microwave Theory and Techniques for the term 2021–2023.